ADVANCED ENERGY MATERIALS
www.advenergymat.de

Design Lithium Exchanged Zeolite Based Multifunctional Electrode Additive for Ultra-High Loading Electrode Toward High Energy Density Lithium Metal Battery

Yunnan Gao, Yi Yang, Tingzhou Yang, Zhen Zhang, Liang Tang, Zhiyu Mao, Yongguang Zhang, Dan Luo,* and Zhongwei Chen**

The practicalization of a high energy density battery requires the electrode to achieve decent performance under ultra-high active material loading. However, as the electrode thickness increases, there is a notable restriction in ionic transport in the electrodes, limiting the diffusion kinetics of Li^+ and the utilization rate of active substances. In this study, lithium-ion-exchanged zeolite X (Li-X zeolite) is synthesized via Li^+ exchange strategy to enhance Li^+ diffusion kinetics. When incorporated Li–X zeolite into the ultra-high loading cathodes, it possesses i) high electron conductivity with a uniform network by reducing tortuosity, ii) decent ion conductivity attributes to modulated Li^+ diffusivity of Li-X and iii) high elasticity to prevent particle-level cracking and electrode-level disintegration. Moreover, Li–X zeolite at the solid/liquid interface facilitates the formation of a stable cathode electrolyte interface, which effectively suppresses side reactions and mitigates the dissolution of transition cations. Therefore, an ultra-high loading (66 mg cm^{-2}) cathode is fabricated via dry electrode technology, demonstrating a remarkable areal capacity of 12.7 mAh cm^{-2} and a high energy density of 464 Wh kg^{-1} in a lithium metal battery. The well-designed electrode structure with multifunctional Li–X zeolite as an additive in thick cathodes holds promise to enhance the battery's rate capability, cycling stability, and overall energy density.

1. Introduction

Lithium-ion batteries (LIBs) play a vital role in storing energy and powering electric vehicles (EVs), thereby mitigating the CO_2 emissions associated with traditional fossil fuel-powered vehicles.[1,2] To address the issue of electric vehicle range and improve energy density, increasing the active material loading of electrodes is a crucial direction in battery development to enhance the energy density of LIBs. This approach effectively reduces the proportion of non-active substances such as the current collector, electrode tabs, and battery casing.[3] Nevertheless, traditional manufacturing of LIB electrodes involves the use of N-methyl pyrrolidone (NMP) as a solvent for cathodes. This wet-film approach leads to electrode cracking in thick electrodes and results in high energy consumption during the drying process.[4,5] Therefore, there is an urgent need for an advanced LIB electrode processing method for high-loading electrodes.

The dry process is well-suited for fabricating thick electrodes with ultra-high mass loading to increase the energy density of the battery.[6] However, as the electrode thickness increases, there is a notable restriction in ionic transport in the electrodes, limiting the diffusion kinetics of lithium ions and resulting in a decrease in the utilization rate of active substances.[7,8] The well-percolated ion/electron transport pathways can be achieved by implanting a certain amount of solid-state electrolyte into the electrodes.[9,10] Moreover, the infiltration of electrolytes also plays a pivotal role in thick electrodes. Incomplete wetting has the potential to create "dead electrode zones," which may contribute to the formation of dendrites, causing short circuits and diminishing the overall cycle life of batteries.[11,12] Hence, the design and optimization of electrode structure for thick electrodes with high loading have become crucial technical approaches to enhance energy density.

The lithium-ion-exchanged zeolite X (Li-X zeolite) showed great potential in energy-storage systems.[13,14] In this study, we synthesized Li-X zeolite via Li^+ exchange strategy. Density functional theory (DFT) calculations investigated the distinctive structure's impact on the adsorption and storing behavior of Li^+, which indicated the promising performance of Li-X as a solid-state electrolyte for applications requiring high-performance ion storage and rapid charge-discharge capabilities. Furthermore, we employed the binder fibrillation process to manufacture a $LiNi_{0.8}Co_{0.1}Mn_{0.1}O_2$ (NMC811) electrode with ultrahigh loadings

Y. Gao, Y. Yang, T. Yang, Z. Zhang, L. Tang, Z. Mao, Y. Zhang, D. Luo, Z. Chen
Power Battery & System Research Center & State Key Laboratory of Catalysis
Dalian Institute of Chemical Physics
Chinese Academy of Sciences Dalian
Dalian, Liaoning 116023, P. R. China
E-mail: ygzhang@dicp.ac.cn; luodan@dicp.ac.cn; zwchen@dicp.ac.cn

The ORCID identification number(s) for the author(s) of this article can be found under https://doi.org/10.1002/aenm.202403063

DOI: 10.1002/aenm.202403063

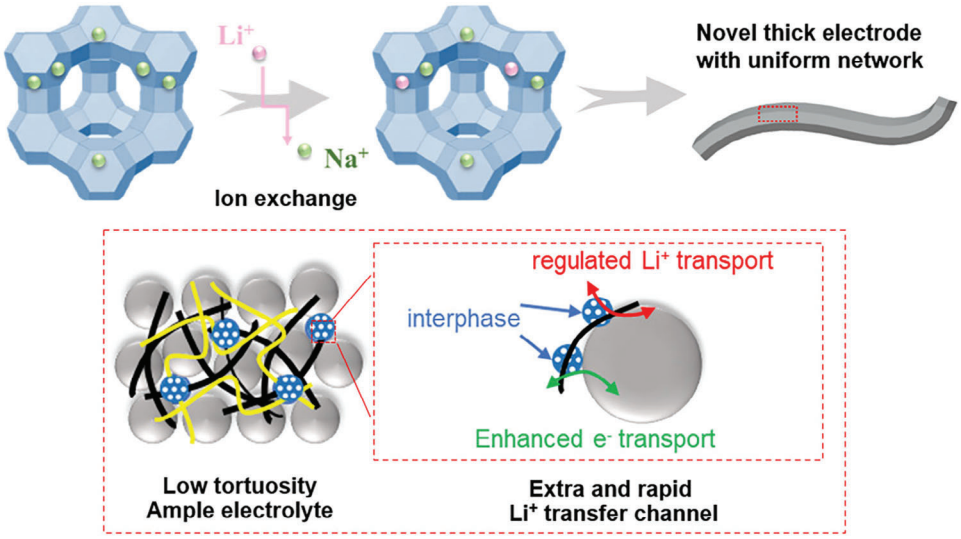

Figure 1. Schematic of the preparation of the Li–X zeolite.

(≈66 mg cm^{-2}). To address the aforementioned challenges, we have introduced Li–X zeolite as a multifunctional additive to the cathode. The optimally composed dry film with Li–X multifunctional additives (DF/LiX) is compared with dry film (DF). The incorporation of Li–X as a solid-state electrolyte i) enhances electrolyte infiltration by increasing electrode porosity (ε), ii) accelerates electron conduction by reducing electrode tortuosity (τ) and iii) regulates ion transport by providing extra and rapid ion transfer channel, as shown in **Figure 1**. As a result, a remarkably high areal capacity of 12.7 mAh cm^{-2} and a high energy density pouch cell of 464 Wh kg^{-1} are obtained, holding great potential to be used for practical Li-metal batteries (LMBs).

2. Results and Discussion

2.1. Properties Characterization of Li–X Zeolite

As depicted in Figure 1, the Li–X zeolite was synthesized through immersing Na–X zeolite in a concentrated solution of LiCl for the exchange of Li to Na ions. In **Figures** 2a and S1 (Supporting Information), the X-ray diffraction (XRD) patterns for Na–X and Li–X zeolites are presented. The main diffraction peak of the materials corresponds to $Na_2Al_2Si_{2.5}O_9{\cdot}6.2H_2O$ (JCPDS #38–2073), indicating that the Li-X zeolite extends the structure of Na-X zeolite during the exchange of Na with Li ions. Furthermore, following the exchange of Li ions, the Bragg reflection shifted to higher 2θ angles, and the intensity of the peak increased, suggesting the successful introduction of Li ions with a smaller radius than Na ions. The results of X-ray photoelectron spectroscopy (XPS) further confirmed the successful introduction of Li ions (Figure 2b). The ion-exchange capability of zeolites is fundamentally linked to the number and activity of cationic sites, which can be regulated by tailoring the Si/Al ratio and allocation of the zeolite matrix, respectively. The low silicon-to-aluminum ratio of X zeolite leads to a limited concentration of negative charges due to the aluminum-oxygen tetrahedra, which requires a limited quantity of exchangeable cations to balance these charges and ensure the stability of the structure.[15,16] The results from the inductively coupled plasma optical emission spectrometer (ICP-OES) (Table S1, Supporting Information) further confirmed Li cation replacement with the content of 2.27%, and the decrease in the Si/Al ratio favored cation adsorption during the cycling of batteries. Both Na–X and Li–X zeolite composites exhibited a type I N_2 adsorption/desorption isotherm, shown as the BDDT (Brunauer–Deming–Deming–Teller) classification (Figure 2c). The Li–X zeolite exhibits an increased surface area of 720 m^2 g^{-1} compared to the 680 m^2 g^{-1} observed in Na–X. The micropores with a pore size of 1.7 nm and several mesopores with a pore size of 4–6 nm indicate that Li–X retained a well-bridged porous conductive skeleton. To validate the morphology of zeolites, the scanning electron microscopy (SEM) image (Figure 2d) of Li–X exhibits a polyhedral morphology with crystallite sizes of ≈1 µm, consistent with that of Na–X. This suggests that Li–X maintains the stable structure of Na–X after the cation exchange. The high-resolution transmission electron microscopy (HRTEM) image (Figure 2e) of Li–X reveals a lattice spacing at 1.3 nm, in line with the (111) zeolite lattice. Compared with Na-X, the smaller lattice spacing after Li exchange is in accord with the result of XRD, indicating the successful introduction of Li ions into Na-X zeolite.

DFT calculations were employed to thoroughly investigate the distinctive structure's impact on the adsorption and storing behavior of Li ions. The models of Na-X and Li–X were constructed according to the ratios of ICP results. From the perspective of lattice dimensions (Table S2, Supporting Information), the optimized model structure of Li-X (Figure 2f) is of similar lattice constants and porous structures with Na-X zeolite (Figure S2, Supporting Information). The adsorption energy (E_{ads}) of Li^+ of Li-X and Na-X was calculated to be −3.4 and −1.8 eV, respectively, indicating stronger adsorption and interaction between Li^+ and Li-X compared to Na-X. The different adsorption morphology, that is, three-coordinate configuration formed by Li^+ and three oxygen atoms in Li-X, a two-coordinate configuration in Na-X, leads to their significant difference in Li^+ adsorption

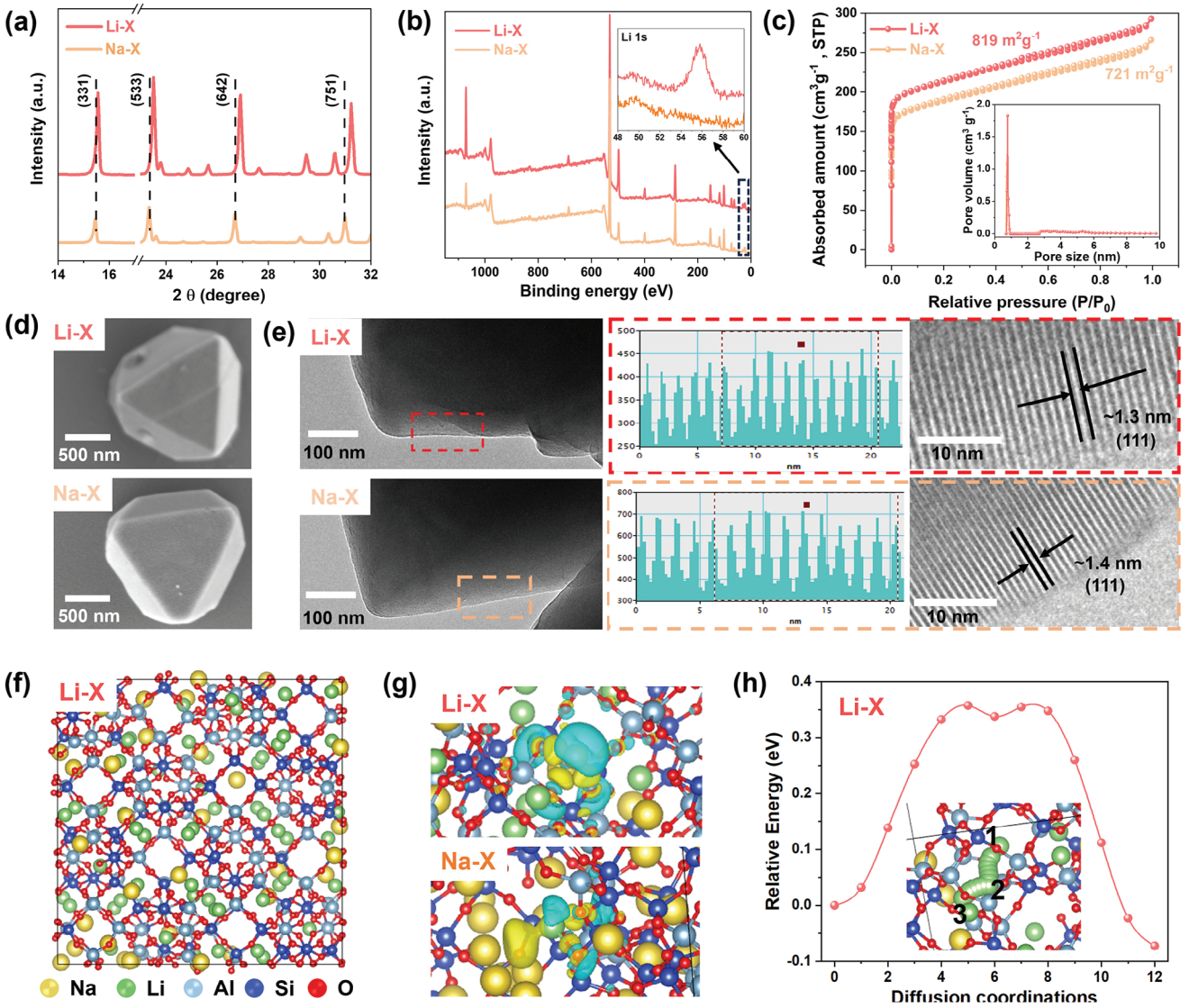

Figure 2. a) The XRD patterns, b) The XPS survey and Li 1s HRXPS spectra, c) N_2 adsorption-desorption isotherms and pore-size distributions, d) SEM images, e) HRTEM images of Li-X and Na-X zeolite. The squares in e illustrate the distance of the plane. f) The simulation model of Li-X zeolite, yellow for Na, green for Li, white for Al, mazarine for Si, red for O. g) Charge density difference of Li-X and Na-X, in which yellow and cyan represent charge accumulation and depletion, respectively. h) The migration path of Li^+ in Li-X and corresponding diffusion energy barriers.

energy. In addition, the more charge transfer from Li^+ to Li-X (0.92 |e|) than to Na-X (0.45 |e|) is obtained by Bader charge analysis and charge density difference (Figure 2g). The robust interaction in the Li-X provided an optimal environment for the efficient adsorption of Li^+, enhancing the diffusion kinetics of Li^+.[17] The Li^+ migration process in Li-X (Figure 2h), involving the Li^+ located at site 1 hops into the adjacent unoccupied site 2, and then hops into the subsequent site 3 are discussed, and the corresponding migration barrier is 0.36 eV, which is a value comparable to typical modes observed in solid-state electrolytes reported previously.[18] Therefore, the Li^+ adsorption and migrations behavior observed in Li-X indicate promising performance as a solid-state electrolyte for applications requiring high-performance ion storage and rapid charge-discharge capabilities.

2.2. Properties Characterization of Dry-Film Electrodes

Dry-film cathodes were produced using the binder fibrillation method. After the introduction of Li-X, the SEM-EDX elemental mapping images (Figure S3, Supporting Information) illustrate the uniform distributions of Li-X on the surface of NMC811. The SEM image of the DF electrode (Figure S4, Supporting Information) displays NMC811 spherical particles and uneven filiform. In contrast, the DF/LiX electrode (**Figure 3**a) prominently showcases the elongated PTFE fibers with random nodules and branched structure. Figure S4 (Supporting Information) exhibited the particles of Li-X zeolite distributed on the PTFE fiber, which interlock with carbon and NMC811, forming strong anchorage points, resulting in improved tensile strength (Figure S6, Supporting Information). The prepared electrodes underwent

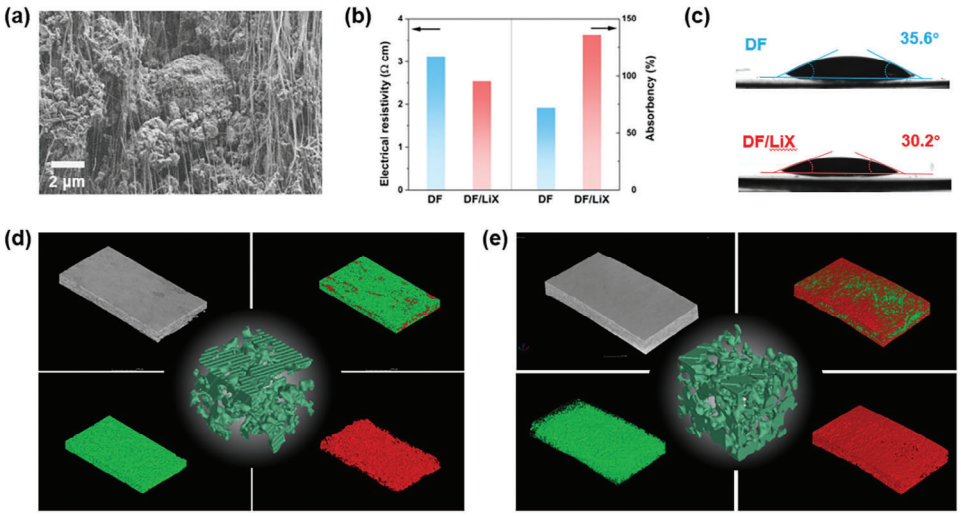

Figure 3. a) SEM image of DF/LiX. b) Electrical resistivity and absorbency of electrolytes of DF and DF/LiX electrodes. c) Contact angles of DF/LiX and DF electrodes. Micro-CT images of the d) DF and e) DF/LiX electrodes. NCM811 is labeled green, and carbon is labeled red. (inside) 3D electrode structures of DF and DF/LiX reconstructed from X-ray nanotomography.

folding to assess their brittleness (Figure S6, Supporting Information **inside**), which indicated the homogeneously distributed PTFE fibrils and a tightly intertwined network of the electrode. Furthermore, the results of the pull-off test (Figure S7, Supporting Information) showed the cohesive strength of the dry electrode surpassed that of the wet electrode, suggesting superior cohesion and synergistic interaction between VGCF and PTFE. The electrode porosity (ε) was calculated by Equation S1 (Supporting Information). In comparison to the ε of DF (28.23%), the ε of DF/LiX is 32.01%, indicating that the introduction of porous zeolite increases the ε of the electrode. The BET (Brunauer–Emmett–Teller) results (Figure S8, Supporting Information) confirm the effect of porous zeolite. The surface area of DF/LiX is determined to be 17.58 $m^2\ g^{-1}$, higher than that of DF, which has a surface area of 13.84 $m^2\ g^{-1}$. The introduction of porous zeolites in the electrode decreased the surface electrical resistivity and enhanced the absorbency of the electrolyte (Figure 3b). The contact angle test with the electrolyte was further confirmed the effect of porous additives. As shown in Figure 3c and Figure S9 (Supporting Information), the smaller contact angle of DF/NaX (32.5°) compared to that of DF (35.6°) indicates that the introduction of porous additive induced better electrolyte infiltration. With the larger surface area than Na–X, the DF/LiX (30.2°) showed a smaller contact angle than DF/NaX, suggesting the better electrolyte infiltration. This improvement increases the total electrochemically active surface area and decreases dead electrode zones, further enhancing the cell energy and power capability.

To elucidate the internal structures of the electrodes, micro-computed tomography (micro-CT) was employed for comparative analysis of the DF and DF/LiX electrodes (Figure 3d,e). The resulting 3D images exhibited two distinct phases based on their significant disparity in absorption contrast: an active material phase (NMC811, depicted in green) and a carbon phase (Carbon, represented in red).[19] The DF and DF/LiX electrodes with a dense and compact arrangement of the active materials and carbon structure, provided evidence for the presence of a robust conductive framework with minimal cracks. However, in comparison to DF, the surface of DF/LiX showed more conductive carbon, which could function as a protective layer for NMC,[20] and decrease the surface electrical resistivity of DF/LiX, according with Figure 3b. Tortuosity (τ) represents the actual flow path of the electrolyte in porous electrodes, playing a crucial role in Li^+ diffusion and the rate performance of batteries. We measured the τ of DF/LiX (4.67) and DF (5.52) independently by reconstructing the electrode microstructures from 3D nanotomography measurements (Figure 3d,e inside). The computed τ only reflects the pore space between NMC811 without considering carbon and PTFE, which are transparent to X-rays used in the micro-CT technique. To further investigate the cause of the tortuosity difference, more accurate electrochemical impedance measurements using symmetrical cells are conducted.[21,22] Figure S10 (Supporting Information) shows that DF/LiX has a much lower τ than DF (5.15 vs 7.14), which is calculated using Equation S2 (Supporting Information). The lower τ values align with the porous structure of DF/LiX, where more open and penetrating pores could be observed, as characterized above. In summary, the thick electrodes with porous Li–X zeolite exhibited a conductive intertwined network. Furthermore, Li-X additives play a crucial role in influencing the ion transport of the electrolyte within the electrode network by increasing the porosity and lowering the tortuosity.

2.3. Electrochemical Performance of High-Loading Electrodes

The electrochemical performance of DF and DF/LiX are exhibited in **Figure 4**. The Nyquist plot of the three electrodes (Figure S11, Supporting Information) showed that DF/LiX and DF/NaX demonstrate lower R_{ct} than DF, indicating the porous structure of the electrode decreases the impedance. DF/LiX with Li cations located in the extra-framework further improved the Li^+ transportation and decreased the impedance, compared with DF/NaX. The cyclic voltammograms (CV) plots (Figure 4a) display a smaller peak voltage difference of DF/LiX of 0.15 V compared to 0.18 V for the DF, suggesting reduced polarization and improved

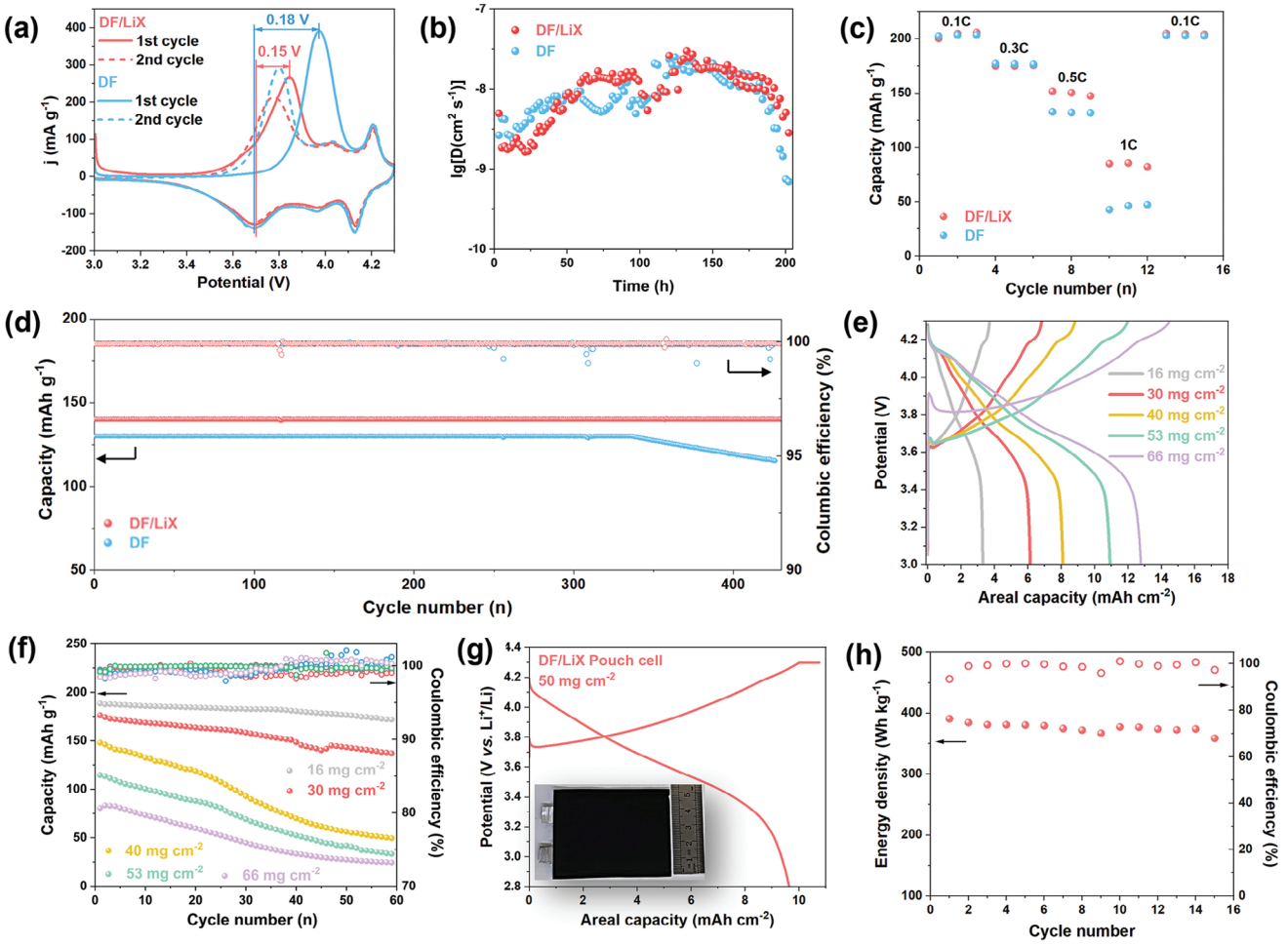

Figure 4. a) CV plots of the DF and DF/LiX, respectively. b) D_{Li+} values of DF and DF/LiX. c) Rate capability at different current densities of 0.1, 0.3, 0.5, and 1 C in a voltage range of 3.0–4.3 V. d) Cycling performance of the DF and DF/LiX at a charge/discharge current density of 1.0 C at a voltage range of 3.0–4.3 V. e) Charge/discharge voltage profiles (in terms of areal capacities) with different areal mass loadings at 0.1 C. f) Cycling performance of the DF/LiX with different areal mass loadings at 0.5 C at a voltage range of 3.0–4.3 V. g) Charge/discharge voltage profile of the Li-metal DF/LiX pouch cell at 0.05 C. (inside) The image of the pouch cell. h) Cycling performance of the Li-metal DF/LiX pouch cells at 0.1 C.

electrochemical kinetics in the DF/LiX electrode.[23,24] The galvanostatic intermittent titration technique (GITT) was employed to understand the behavior of ion transportation (Figure S12, Supporting Information). As displayed in Figure 4b, based on the calculation of GITT, DF/LiX exhibited a higher diffusion coefficient (1.90×10^{-8} cm^2 s^{-1}) than DF (1.55×10^{-8} cm^2 s^{-1}), indicating that DF/LiX has faster ionic transportation. The enhanced lithium diffusivity and reduced impedance growth contribute to the improved battery performance. As shown in Figure 4c, at a low rate of 0.1 C, the coin cells with DF and DF/LiX all deliver a discharge capacity of ≈204 mAh g^{-1}. The DF/LiX coin cell shows a discharge capacity of 181.1 and 142.7 mAh g^{-1} at the current density of 0.5 C and 1 C, respectively, which is higher than that of DF with a capacity of 181.2 and 125.0 mAh g^{-1}. In comparison to DF, DF/LiX demonstrates improved rate performance, particularly at the high rate. Notably, the DF/LiX enables high coulombic efficiency (CE%) of 92.9% during the first cycle, while DF can only reach 84.5% (Figure S13, Supporting Information), due to the side reactions between PTFE and lithium at low potential.[25] The Li-X zeolite with extra Li-ion can replenish the consumption of Li during the side reactions with PTFE, resulting in a higher CE% than DF. Considering the capacity degradation of thick cathodes, the extended cycling was tested at the mass loading of 10 mg cm^{-2}. As shown in Figure 4d, the DF/LiX cathodes are significantly enhanced by the incorporation of Li-X. The DF/LiX electrode maintains almost 99.9% of its capacity (140.1 mAh g^{-1}) at 1C after 400 cycles, while only 88.7% is retained for the DF. It is supposed that Li–X with high ionic conductivity offers additional pathways for Li diffusion, which is crucial for the homogenization of Li-ion.[26] As a result, the DF/LiX cathode with high Li^+ diffusivity and low impedance boosts the rate capability and cycling performance impressively.

High-loading electrodes play a crucial role in improving the battery's performance. As shown in Figure 4e, as the mass loading increases, the areal capacities of all the electrodes also increase. The DF/LiX electrodes, even with mass loadings as high as 66 mg cm^{-2}, still delivered a high capacity of 192 mAh g^{-1}, enabling high areal loading up to 12.7 mAh cm^{-2}. This correlation

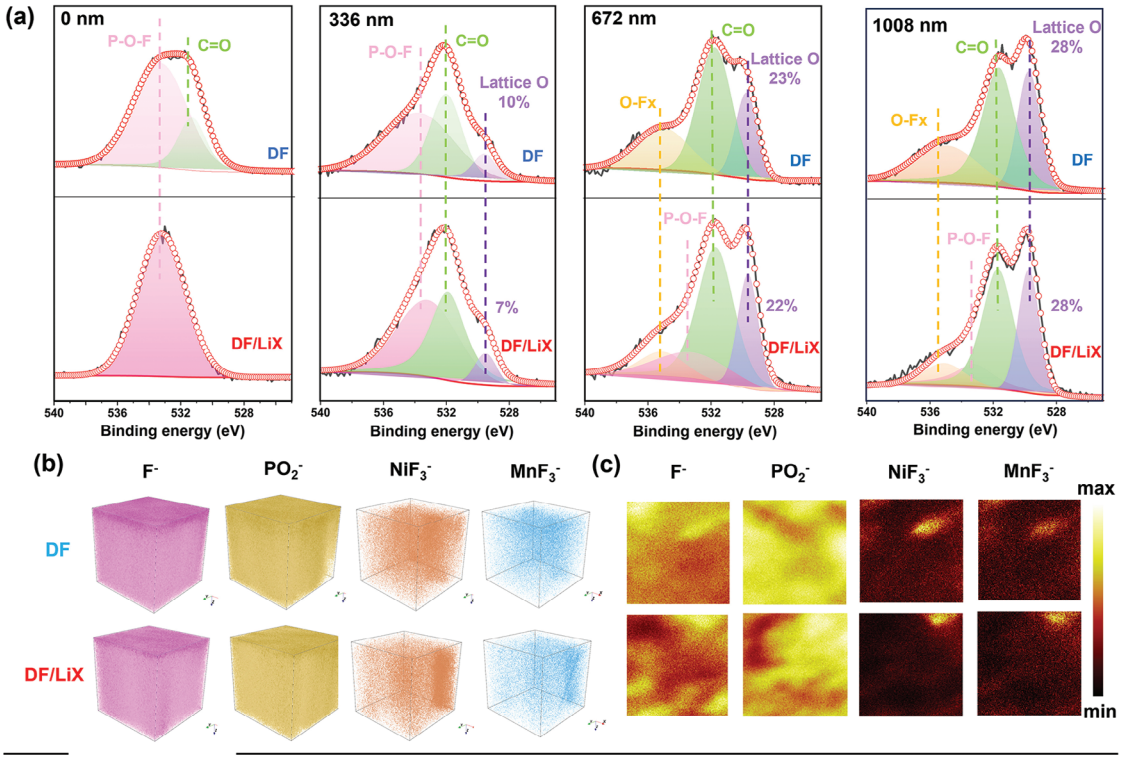

Figure 5. a) O 1s XPS spectra of DF and DF/LiX were collected from the cathode surface with Ar^+ etching at various skin depths. b) The 3D views, c) chemical imaging of ToF-SIMS for F^-, PO_2^-, NiF_3^- and MnF_3^- in DF and DF/LiX.

highlights the potential to improve the capacity of cathodes by optimizing mass-loading parameters. The cycling performances at the rate of 0.5C (Figure 4f) show that the electrodes with mass loading of 16–30 mg cm^{-2} demonstrated consistent cyclic stability over the testing cycles. When the mass loading increases to 40 mg cm^{-2}, the thickness of the electrode contributes to the limited ion/electron transfer, poor kinetics, and high impedance, leading to the decay of capacity.[27,28] However, at a low rate of 0.1 C, with the slow transmission of ion/electron, the electrodes with a high mass loading of 66 mg cm^{-2} exhibited a stable cycling performance, as depicted in Figure S14 (Supporting Information).

A Li||DF/LiX pouch cell (40 × 60 mm^2 in size) was assembled with Li metal (20 µm) and DF/LiX (50 mg cm^{-2}) (Figure 4g). The pouch cell exhibited an initial discharge capacity of 193 mAh g^{-1} at 0.05 C, corresponding to an areal capacity of 9.7 mAh cm^{-2} and an energy density of 464 Wh kg^{-1} calculated based on the entire cell weight. However, the breakdown of Li metal, which becomes dark and rough on the surface (Figure S15, Supporting Information), leads to limited cycling. A pouch cell assembled with DF/LiX (28 mg cm^{-2}) and Li-metal anode (100 µm) was evaluated for cycling performance. As shown in Figure 4h, the result showed the cyclability of the DF/LiX with a capacity retention of 97%. The specific energy, calculated including the cell package weight, was 390 Wh kg^{-1} (Table S3, Supporting Information). The cycle life of Li metal batteries is limited by the dendrite growth and continuous reactions between Li and electrolytes.[29] Further research directions are to enhance the performance of Li metal anodes, such as protection of anodes for inhibition of dendrite formation, electrolyte formula to regulate SEIs, all-solid-state LMBs, and so on.[30,31] In addition, the full cell assembled with graphite as the anode showed a capacity retention of 98% over 100 cycles (Figure S16, Supporting Information), indicating the great stability of DF/LiX cathodes.

2.4. Analysis of the Cycled Cathodes

To better understand the impact of interphase properties, we characterized the CEI (cathode-electrolyte interphase) products from electrodes after 100 cycles. As presented in the XRD pattern of cycled electrodes (Figure S17, Supporting Information), the DF/LiX exhibits robust structural stability with well-maintained crystallinity of NCM811 (JCPDF#87-1553). In addition, EIS results (Figure S18, Supporting Information) showed that the DF/LiX sample has lower R_{ct} than the DF sample after cycling, indicating the better electrochemical activity of DF/LiX, attributable to the beneficial effects of the Li-X zeolite. From the F 1s spectra of the XPS result (Figure S19, Supporting Information), the intensity of the P-F-O peak (686.7 eV) in the cycled DF/LiX is higher than that in the cycled DF. It is worth noting that organic species of P-compounds, primarily originating from the decomposition of solvents and salts in the electrolyte, tend to accumulate on the surface of CEI.[32] This implies that the CEI of DF/LiX is better formed to fully cover the NMC811 surface than DF, as illustrated in Figure S20 (Supporting Information), with large variations in thickness ranging from 3 to 7 nm. XPS-related Ar^+ sputtering depth analysis (**Figure 5a**) shows that no signals from the lattice oxygen (529.7 eV) of NMC in the O 1s region

can be observed due to the shielding by the homogeneous CEI layer. Through the stripping of the CEI layer during Ar^+ etching, the lattice oxygen peak is gradually exposed. At the depth of 672 nm (after 600 s of Ar^+ etching), the intensity of the P-F-O peak still existed in DF/LiX, while it disappeared in DF, indicating that the electrolyte immersed repletely in DF/LiX, in accord with the results of the contact angle. In this case, the released nucleophilic O_2^- reacts with the PTFE, resulting in the formation of the O-F_x composites. For NMC811 materials with high nickel content, the transition metal is easy to dissolve into electrolyte due to the cationic mixing and oxygen evolution.[33] We tested the content of metal in the electrolyte and on the Li metal after cycling by ICP-OES (Figure S21, Supporting Information). Li-X zeolite is introduced to form a positive electrode interface film on the surface, which effectively inhibits the dissolution of transition metal elements and improves cycling performance.

Time-of-flight secondary ion mass spectrometry (TOF-SIMS) analysis (sputtering rate was 1.12 nm s^{-1} for 1200 s) is employed to further elucidate the surface compositions of DF and DF/LiX and reveal the CEI film after cycling.[34] Interactions with organic electrolytes lead to surface structural degradation and the generation of transition metal fluorides (e.g., NiF_3^- and MnF_3^-) inside the CEI film.[35] However, the quantity of F^-, PO_2^-, NiF_3^-, and MnF_3^- species identified in the CEI film of DF/LiX cathodes is significantly lower compared to those observed in DF (Figure S22, Supporting Information). 3D rendering (Figure 5b) and TOF-SIMS chemical imaging (Figure 5c) show the accumulated signals of F^-/PO_2^- and NiF_3^-/MnF_3^- on the surfaces of DF and DF/LiX, revealing the presence of degradation-induced fragments. This suggests that the thick CEI layer in DF/LiX effectively mitigates cathode/electrolyte side reactions and alleviates the dissolution of transition cations, contributing to enhanced stability and reduced degradation. Furthermore, the structural stability of the materials was examined through focused ion beam scanning electron microscopy (FIB-SEM) images (Figure S23, Supporting Information). Several cracks can be observed in cycled DF cathodes, which may facilitate increased parasitic reactions and impedance, subsequently resulting in capacity fading.[36] In contrast, the cycled DF/LiX cathode exhibited smaller cracking along grain boundaries, indicating increased robustness against structural degradation. As a result, Li-X zeolite distributed on the surface of NMC811 served as a buffer layer between the active materials and electrolyte, contributing to the favorable formation of CEI, the dissolution of metal elements, and the structural integrity, further enhancing the battery's performance.

3. Conclusion

In this study, we synthesized Li-X zeolite via the Li^+ exchange method. The results of DFT calculations showed that Li-X with the robust interaction and migrations behavior enhanced the diffusion kinetics of Li^+, indicating the promising performance as a solid-state electrolyte. The porous Li-X zeolite was incorporated in ultrahigh-loading cathodes, which facilitated a uniform network and improved electrolyte infiltration by increasing electrode porosity (ε). The Li-X also accelerated electron conduction by reducing electrode tortuosity (τ). Furthermore, Li-X zeolite acting as a solid-state electrolyte provided extra lithium diffusion channels/pathways that can homogenize Li ion fluxes during lithiation and facilitated the formation of a comprehensive CEI layer at the solid/liquid interface. This effectively suppressed cathode/electrolyte side reactions and mitigated the dissolution of transition cations, further against structural degradation. Benefitting from the advantages, the DF/LiX cathodes exhibited superior rate and cycling performance, in comparison to DF. Even with mass loadings as high as 66 mg cm^{-2}, the DF/LiX electrodes, still delivered a high capacity of 192 mAh g^{-1}, enabling high areal loading up to 12.7 mAh cm^{-2}. Additionally, high-loading pouch cells of DF/LiX, with a capacity of 9.7 mAh cm^{-2}, were fabricated, demonstrating a remarkable energy density of 464 Wh kg^{-1}, inclusive of the cell package weight. Considering the breakdown of Li anode and cycling performance, the specific energy of pouch cells of DF/LiX controlled to 390 Wh kg^{-1}, showing stable cycling performance. The success achieved at the pouch-cell level suggests promising possibilities of Li-X for high-loading electrodes to enhance energy density. This methodology could be extended to other additives (such as porous solid-state electrolyte, Li-exchange MOF, and so on), which can be added to other cathode materials, such as Li-rich layer oxide. Furthermore, the compatibility of additives makes the dry electrode technology a promising solution for the scalable manufacturing of ultrahigh-loading electrodes to achieve the practicalization of high-energy density batteries.

Supporting Information

Supporting Information is available from the Wiley Online Library or from the author.

Acknowledgements

The authors would like to acknowledge the financial support from the Strategic Priority Research Program of the Chinese Academy of Sciences (XDB0600400), Dalian Revitalization Talents Program (no:2022RG01), the National Natural Science Foundation of China (22309179), the Vacuum Interconnected Nanotech Workstation (Nano-X), and the Energy Revolution S&T Program of Yulin Innovation Institute of Clean Energy, Grant no. E411130705.

Conflict of Interest

The authors declare no conflict of interest.

Data Availability Statement

The data that support the findings of this study are available from the corresponding author upon reasonable request.

Keywords

dry electrode technology, high energy density, lithium exchanged zeolite, lithium–metal battery

Received: July 13, 2024
Revised: August 20, 2024
Published online:

[1] U.-H. Kim, G.-T. Park, B.-K. Son, G.-W. Nam, J. Liu, L.-Y. Kuo, P. Kaghazchi, C. S. Yoon, Y.-K. Sun, *Nat. Energy* **2020**, *5*, 860.
[2] A. K. Vinayak, Z. Xu, G. Li, X. Wang, *Renewables* **2023**, *1*, 294.
[3] W. Lu, A. Jansen, D. Dees, P. Nelson, N. R. Veselka, G. Henriksen, *J. Power Sources* **2011**, *3*, 1537.
[4] Y. Liu, X. An, K. Yang, J. Ma, J. Mi, D. Zhang, X. Cheng, Y. Li, Y. Ma, M. Liu, F. Kang, Y.-B. He, *Environ Sci* **2024**, *17*, 344.
[5] Y. Lu, C. Z. Zhao, H. Yuan, J. K. Hu, J. Q. Huang, Q. Zhang, *Matter* **2022**, *5*, 876.
[6] W. Yao, M. Chouchane, W. Li, S. Bai, Z. Liu, L. Li, A. X. Chen, B. Sayahpour, R. Shimizu, G. Raghavendran, M. A. Schroeder, Y.-T. Chen, D. H. S. Tan, B. Sreenarayanan, C. K. Waters, A. Sichler, B. Gould, D. J. Kountz, D. J. Lipomi, M. Zhang, Y. S. Meng, *Energy Environ. Sci.* **2023**, *16*, 1620.
[7] Y. Kuang, C. Chen, D. Kirsch, L. Hu, *Adv. Energy Mater.* **2019**, *9*, 1901457.
[8] H. Li, Y. Tao, X. Zheng, J. Luo, F. Kang, H.-M. Cheng, Q.-H. Yang, *Environ Sci* **2016**, *9*, 3135.
[9] S. Choi, M. Jeon, J. Ahn, W. D. Jung, S. M. Choi, J.-S. Kim, Y.-J. Jang, H.-G. Jung, J.-H. Lee, B.-I. Sang, H. Kim, *ACS Appl. Mater. Interfaces* **2018**, *10*, 23740.
[10] H. Nakamura, T. Kawaguchi, T. Masuyama, A. Sakuda, T. Saito, K. Kuratani, S. Ohsaki, S. Watano, *J. Power Sources* **2020**, *448*, 227579.
[11] A. Davoodabadi, J. Li, H. Zhou, D. L. Wood, T. J. Singler, C. Jin, *J. Energy Storage* **2019**, *26*, 101034.
[12] A. Banerjee, X. Wang, C. Fang, E. A. Wu, Y. S. Meng, *Chem. Rev.* **2020**, *120*, 6878.
[13] J. Liu, X. Xiao, D. Haddad, Q. Zhang, M. Cai, S. Zeng, *Adv. Mater. Technol.* **2021**, *6*, 2100615.
[14] X. Chi, M. Li, J. Di, P. Bai, L. Song, X. Wang, F. Li, S. Liang, J. Xu, J. Yu, *Nature* **2021**, *592*, 551.
[15] Q. Zhang, S. Gao, J. Yu, *Chem. Rev.* **2022**, *123*, 6039.
[16] Z. Ding, Q. Tang, Y. Liu, P. Yao, C. Liu, X. Liu, J. Wu, M. Lavorgna, *Chem. Eng. J.* **2022**, *433*, 133522.
[17] Y. Tang, G. Li, S. Cui, W. Cui, H. Chong, L. Han, H. Pang, *Adv. Funct. Mater.* **2024**, 2403351.
[18] X. He, Y. Zhu, Y. Mo, *Nat. Commun.* **2017**, *8*, 15893.
[19] L. Vásárhelyi, Z. Kónya, A. Kukovecz, R. Vajtai, *Mater. Today Adv.* **2020**, *8*, 100084.
[20] S. J. Sim, S. H. Lee, B. S. Jin, H. S. Kim, *Sci. Rep.* **2020**, *10*, 11114.
[21] J. Landesfeind, J. Hattendorff, A. Ehrl, W. A. Wall, H. A. Gasteiger, *J. Electrochem. Soc.* **2016**, *163*, A1373.
[22] T.-T. Nguyen, A. Demortiere, B. Fleutot, B. Delobel, C. Delacourt, S. J. Cooper, *NPJ Comput. Mater.* **2020**, *6*, 123.
[23] B. P. Thapaliya, T. Wang, A. Y. Borisevich, H. M. Meyer, X.-G. Sun, M. P. Paranthaman, C. A. Bridges, S. Dai, *Adv. Funct. Mater.* **2023**, *33*, 2302443.
[24] M. Ryu, Y. K. Hong, S. Y. Lee, J. H. Park, *Nat. Commun.* **2023**, *14*, 1316.
[25] W. Liu, X. Huang, G. Li, Z. Wang, H. Huang, Z. Lu, R. Xue, L. Chen, *J. Power Sources* **1997**, *68*, 344.
[26] X. Li, J. Liu, M. N. Banis, A. Lushington, R. Li, M. Cai, X. Sun, *Energy Environ. Sci.* **2014**, *7*, 768.
[27] H. Li, Z. Wu, X. Liu, H. Lu, W. Zhang, F. Li, H. Yu, J. Yu, B. Zhang, Z. Xiong, Y. Tao, Q. H. Yang, *Natl. Sci. Rev.* **2024**, *11*, nwae207.
[28] X. Wu, S. Xia, Y. Huang, X. Hu, B. Yuan, S. Chen, Y. Yu, W. Liu, *Adv. Funct. Mater.* **2019**, *29*, 1903961.
[29] Y. Ji, Z. Wang, C. Zhao, Z. Fang, Y. Gong, Q. Jing, Y. Xia, T. Luan, Y. Jiang, J. Liang, X. Li, M. Zhao, X. Zhai, X. Bie, T. Jiang, D. Geng, X. Sun, *Renewables* **2024**, *2*, 194.
[30] Y. Guo, S. Pan, X. Yi, S. Chi, X. Yin, C. Geng, Q. Yin, Q. Zhan, Z. Zhao, F.-M. Jin, H. Fang, Y.-B. He, F. Kang, S. Wu, Q.-H. Yang, *Adv. Mater.* **2024**, *36*, 2308493.
[31] H. Lu, C. Yang, F. Wang, L. Wang, J. Zhou, W. Chen, Q. H. Yang, *Nano Res.* **2023**, *16*, 8321.
[32] Y. Chen, W. Zhao, Q. Zhang, G. Yang, J. Zheng, W. Tang, Q. Xu, C. Lai, J. Yang, C. Peng, *Adv. Funct. Mater.* **2020**, *30*, 2000396.
[33] Y. Guo, S. Pan, X. Yi, S. Chi, X. Yin, C. Geng, Q. Yin, Q. Zhan, Z. Zhao, F.-M. Jin, H. Fang, Y.-B. He, F. Kang, S. Wu, Q.-H. Yang, *Adv. Mater.* **2023**, *36*, 2308493.
[34] W. Li, A. Dolocan, P. Oh, H. Celio, S. Park, J. Cho, A. Manthiram, *Nat. Commun.* **2017**, *8*, 14589.
[35] Y. Sun, T. Yang, H. Ji, J. Zhou, Z. Wang, T. Qian, C. Yan, *Adv. Energy Mater.* **2020**, *10*, 2002373.
[36] H.-H. Ryu, K.-J. Park, C. S. Yoon, Y.-K. Sun, *Chem. Mater.* **2018**, *30*, 1155.